



Panoramic Imaging Assessment of Different Bladder Phantoms – An Evaluation Study

Ralf Hackner, Rodrigo Suarez-Ibarrola, Tian Qiu, Niels Lemke, Philipp-Fabian Pohlmann, Konrad Wilhelm, Peer Fischer, Arkadiusz Miernik, and Thomas Wittenberg

OBJECTIVE	To evaluate “panoramic image stitching” for cystoscopy, a novel technique to augment a urologist’s field of view transoperatively in real-time during a cystoscopic “keyhole” procedure, 3-D bladder phantoms provide a suitable setting. Thus, the objective is the evaluation of different 3-D printed bladder phantoms with respect to their ability to be used for extended experiments of panoramic cystoscopy.
MATERIALS AND METHODS	Five bladder phantoms with different geometries, surface textures, stiffness and materials were assessed with rigid 0- and 30-degree lenses and a video-cystoscope regarding suitability for image stitching. For panoramic image generation, we use an established real-time stitching approach successfully applied to retrospective cystoscopy image sequences from real clinical cases. For evaluation of the experiments two quality criteria were defined, namely ‘completeness’ (describing the internal area of the phantom that can be stitched), and ‘extension’ (how far does an acquired panorama extend beyond the assumed ‘equator’ of the phantom).
RESULTS	Panoramas of all phantom and endoscope combinations were computed. Using landmarks (south pole, north pole, equator) in the phantoms, maximum extension of the panoramas was assessed. The computed panoramas yield maximum extensions between 270° (0-degree cystoscope) and 330° (video cystoscope). Deformable phantoms yield larger panoramas than the rigid models.
CONCLUSION	It can be concluded that the stitching process works quite well with all evaluated phantoms. Nevertheless, a novel phantom would be needed, combining a deformable, elliptical geometry and real-type vascular texture in the inside, that can be filled with water. UROLOGY 156: e103–e110, 2021. © 2021 Elsevier Inc.

OBJECTIVE

In recent years, we developed a software system to create bladder panoramic images (and other body hollow organs) during endoscopic examinations.¹⁻³ The software computes the image panoramas in real-time, meaning, while the surgeon moves the tip of the endoscope, the panorama is simultaneously computed and displayed on a screen with a very low temporal delay of approximately 60 ms. Such endoscopic image panoramas enlarge a surgeon’s field of view, provide visual feedback if there are yet unobserved areas and improve the quality of lesion documentation.² Fig. 1 (top row) provides an example of

a bladder wall panorama, computed (retrospectively) from a cystoscopy sequence obtained from a routine cystoscopic examination at the University Hospital in Freiburg, Germany. The image processing software, described in detail below, provides a panorama (or mosaic) of the textured bladder wall, by “stitching” together consecutive images of a cystoscopic video stream using visible correspondences (“features”) such as vascular bifurcations.

For the generation of such panoramas, it is important to ensure a certain quality of the acquired images sequences: In case of fast movement or blurry images, the panorama generation cannot be continued. To assist the physician during the real-time stitching, the software system interacts with the user in various ways: Direct visual feedback is provided on the screen in real-time by surrounding the current image frame of the video stream by the already generated panorama, and the user thus is visually requested to move the tip of the cystoscope to a position whose image has not yet been integrated in the panorama to continue the stitching process with new images.

Testing such interactions with retrospective image data as eg, precordered cystoscopic videos from real

Conflict of Interest: There exists no conflict of interest

From the Fraunhofer Institute for Integrated Circuits IIS, Erlangen, Germany; the Department of Urology, Faculty of Medicine, University of Freiburg Medical Centre, Freiburg, Germany; the Cyber Valley Research Group, University of Stuttgart, Stuttgart, Germany; the Max Planck Institute for Intelligent Systems, Stuttgart, Germany; the Schöilly Fiberoptic GmbH, Denzlingen, Germany; and the Chair of Visual Computing, University Erlangen, Germany

Address correspondence to: Thomas Wittenberg, PhD, Fraunhofer Institute for Integrated Circuits IIS, Am Wolfsmantel 33, Erlangen 91054 Germany. E-mail: thomas.wittenberg@iis.fraunhofer.de

Submitted: September 24, 2020, accepted (with revisions): May 19, 2021

© 2021 Elsevier Inc.
All rights reserved.

<https://doi.org/10.1016/j.urology.2021.05.036> e103
0090-4295

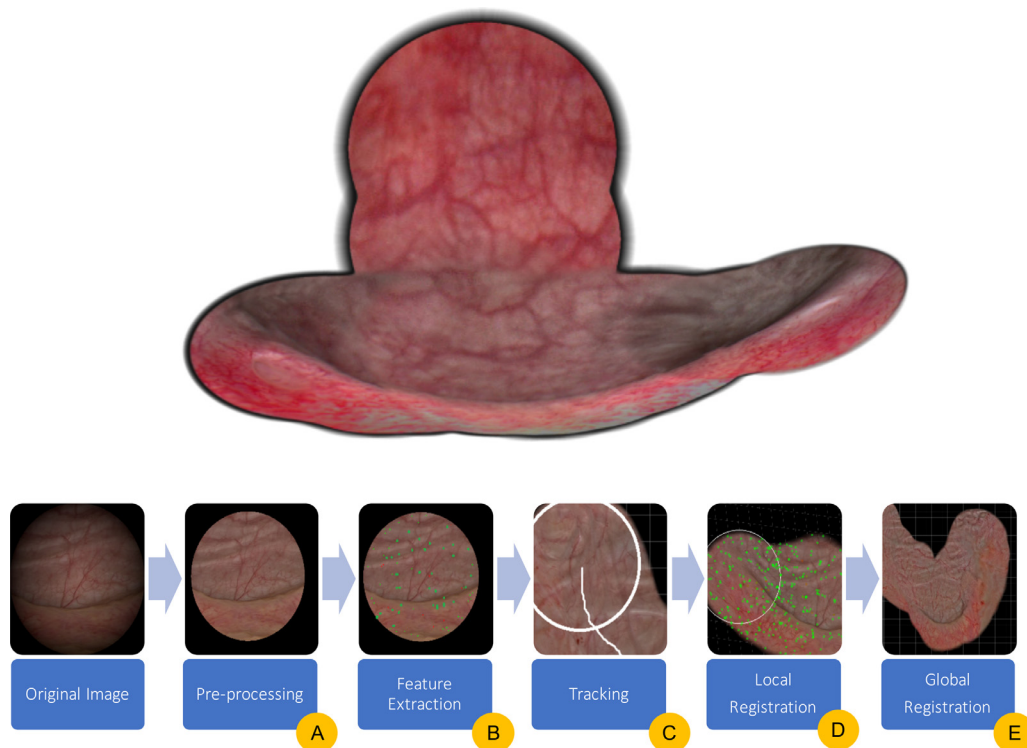


Figure 1. Top: Example of a bladder panoramic image based on a cystoscopic examination from the University Hospital in Freiburg, Germany. Bottom: Overview of the image-processing pipeline for panorama generation.

examinations is hardly possible, since the user can no longer react to yet unknown influences. Additionally, live stitching workflow demonstrations cannot be performed based on prerecorded videos. Furthermore, since such medical assessment software for bladder documentation is considered a medical device under the new medical device regulation (MDR), it is not possible to carry out exhaustive experiments in real patients.

Hence, as an alternative, bladder phantoms can be applied for real-time stitching experiments and demonstrations, made from silicone, rubber and other polymers. An evaluation of such phantoms will help enhance the stitching procedures as well as improve the phantoms to be more realistic.

STATE OF THE ART

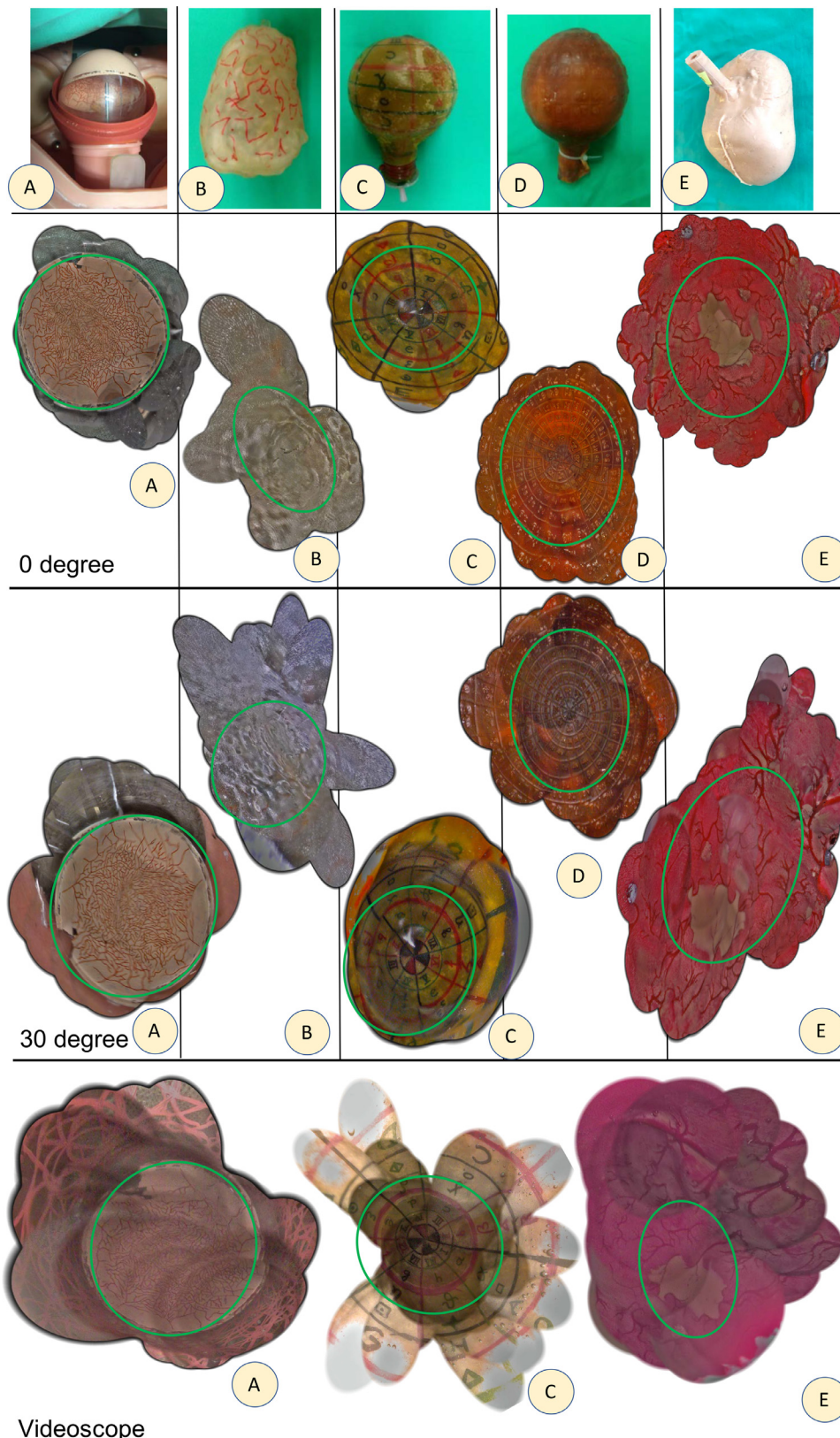
Various bladder phantoms are currently available and applied in the field of Urology. Nevertheless, most of these phantoms serve dedicated clinical purposes, such as education in anatomy, simulation of laser-based interventions, ultrasound imaging assessment or endoscopy training. One necessity for the generation of cystoscopic panorama images is the availability of a tissue-like texture with vascularization or a somehow texturized surface inside the phantom. Since standard cystoscopy phantoms (as eg, the VirtaMed UroSim System,⁴ the CLA bladder phantom,⁵ or the Symbionix UroMentor⁶⁻⁸) do not provide prominent and sufficient bladder wall texture features, several alternative phantoms have been designed, built and

evaluated with respect to panoramic image stitching of cystoscopic video data. Hence, for our research, we used a self-constructed bladder phantom,¹ a 3D-printed bladder phantom,⁹ two silicon phantoms from the University Hospital in Tübingen and a phantom created by the Max Planck Institute for Intelligent Systems <https://link.springer.com/article/10.1007%2Fs10439-021-02793-0#citeas>.²² A phantom similar to our self-constructed one (*phantom A*, Fig. 2A, top row) was also used by Péntek et al¹⁰ for experiments to reconstruct a bladder's 3D-geometry from endoscopic images. Lurie et al¹¹ suggested a 3D-printed multi-layered bladder phantom, which inspired us to construct a less complicated phantom (*phantom E*, see below).

MATERIALS AND METHODS

Phantoms

For our experiments, five bladder phantoms were used,⁹ see Figure 2 (top row) and Table 1 (top part). A prerequisite is for the bladder walls surface to be somehow texturized to provide sufficient information for the stitching algorithm. **Phantom A** is based on an acrylic-glass sphere with a 100 mm diameter and a 1 cm diameter circular opening for the insertion of the cystoscope. The distal hemisphere is colored in pink, and a vascular pattern was added manually, cf. Figure 2A, top row. Only one hemisphere is covered with paint. **Phantom B** is a silicon-based 3D-printed model, see Figure 2B, top row. The 3D data used for printing was obtained from an interactive segmented bladder based on MRI images.¹² After the segmentation, the volumetric



Videoscope

Figure 2. Top row: Bladder phantom images used for the experiments: (A): hand-colored acrylic glass sphere, (B): 3D-printed silicon phantom, (C): hand-colored and hand labelled silicon phantom, (D): silicon bladder phantom with imprinted structures, (E): 3D-printed / molded phantom with imprinted structures. Second row: Panoramic images recorded with a 30-degree cystoscope from the bladder phantoms in the top row, the 'equator' between the distal and proximal hemisphere (cf. Fig. 3) is marked green. Third row: Panoramic images recorded with a 0-degree cystoscope from the bladder phantoms in the top row, the 'equator' between the distal and proximal hemisphere is marked green. Bottom row: Panoramic images acquired with a flexible video-cystoscopy from the bladder phantoms A, C, and E in the top row.

Table 1. Top: Characteristics of the five phantoms used for the experiments; Center: captured maximum range of the angle between the central landmark (“south pole”) and outer-most landmark that can be observed with the endoscope, Bottom: Visible stitching errors in relation to the total number of frames in the panorama image, (additions / changes with resp. to initial submission appear in green).

Characteristics of Phantoms					
	Phantom A	Phantom B	Phantom C	Phantom D	Phantom E
Material	Acrylic glass	3D-printed Silicon	Cast-based Silicon	Cast-based Silicon	3D-molded Silicon
Form	Spherical	Ellipsoid	Spherical	Spherical	Ellipsoid
Diameter [mm]	100	80 -130	85	95	64-112
Stiffness	Stiff	Stiff	Deformable	Deformable	Deformable
Water filling possible	No	no	Yes	yes	yes
Texture	Manually added coarse vascularization	Print artifacts; manually added texture	Manually added lines and symbols	Negative embossed lines and symbols	Printed texture
Captured maximum degree of latitude					
Cystoscope	Phantom A	Phantom B	Phantom C	Phantom D	Phantom E
0 degree	~120°	~60°	~130°	~135°	~130°
30 degree	~120°	~70°	~150°	~135°	~140°
Videoscope	~140°	—	~155°	—	~165°
Visible stitching errors in relation to total number of frames in panorama image					
Cystoscope	Phantom A	Phantom B	Phantom C	Phantom D	Phantom E
0 degree	2 /108	3/155	2/84	7/166	1/320
30 degree	7 /58	14/188	6/87	5/160	6/220
Videoscope	3/162	—	5/153	—	5/48

data was converted to a 3D-mesh, and “holes” or incomplete areas in the bladder wall were closed manually. The location of the “entrance” to the lumen is anatomically correct resembling the urethra. The vascular texture was augmented manually. **Phantom C** (from the Tübingen University Hospital) was fabricated from silicone and is based on a handmade plaster negative. For orientation purposes as well as texture, a grid with eight vertical and eight horizontal lines and a set of 64 different symbols were added manually, cf. [Figure 2C](#), top row. **Phantom D** (also from Tübingen University Hospital) is a variation of phantom C, see [Figure 2D](#), top row. Here the ‘negative’ cast is 3D-printed, where elevated letters and numbers were added to the surface. In the positive silicon-phantom these letters and numbers are depicted in the inside of the phantom and hence provide texture and structures to support the stitching process. Finally, **phantom E**, developed at the Max-Planck-Institute for Intelligent Systems in Stuttgart, is based on a silicon molding technique, originally developed for the manufacturing of kidney phantoms,^{13,14} cf. [Figure 2E](#), top row. The vascular texture is quite realistic, but not as dense as in real tissue, since capillaries are missing. Beside the vessel structure, the phantom also features various types of tumors.

While *phantom A* is static, *phantoms B* to *E* are partially deformable due to soft silicon material. *Phantoms B* and *E* are anatomically correct models in the sense that they are based on volumetric image data, while the other three phantoms approximate the bladder volume as spheres and thus simulate the water-filled state during cystoscopy. A comparison of all phantoms used is provided in [Table 1](#) (top part).

Endoscopic Imaging

For cystoscopic imaging of the above-described bladder phantoms, a state-of-the-art cystoscopy system was used. This system consists of a light source (Richard Wolf, Knittlingen; ENDO-LIGHT Flex LED), a 0-degree 4 mm cystoscope (Richard Wolf, SN 5000321214), a 30-degree 4 mm cystoscope (LUT HDscope, Schölly, Denzlingen; SN552687), an endoscopic video camera (Richard Wolf, ENDOCAM) and an endoscope video platform (Richard Wolf, ENDOCAM Logic HD with Endolight Flex LED). Additionally, a flexible 4 mm video cystoscope (Richard Wolf) was used applied.

Panoramic Image Processing

Recently, we developed a software system which allows the computation and display of large-scale bladder panoramic images in real-time during a diagnostic cystoscopy.^{1,2} The software has been optimized to be used in the bladder,^{1,2} but also works with other spherical and hollow organs.¹⁵⁻¹⁷ The computer equipped with the stitching software is connected to the endoscope controller (see [Section "Endoscopic Imaging"](#)) by a frame-grabber device to acquire a live video stream from the cystoscopy system during the phantom's examination in real time with approximately 25 frames per second. For the image stitching process (cf. [Fig. 1](#), bottom) a five-step image processing pipeline is applied. In *Step A*, the input images are conditioned using pre-processing filters. First, a color-shading correction is performed¹⁸ in order to equalize the heterogeneous endoscopic illumination. Furthermore, and in extension of our previous work,⁹ an internal down-scaling of the HD images to obtain an image pyramid is computed using a bilinear interpolation scheme from pyramid layer n to layer $n + 1$. In contrast to Gaussian filtering, bilinear interpolation preserves edges and corners, both strongly needed for the feature-based local registration step. The preprocessing

step is then followed by a feature extraction process (*Step B*). For the tracking process (*Step C*) and the registration (*steps D and E*), we use SURF (“speeded up robust features”) features and key points.¹⁹ These features are a common technique to detect prominent landmarks, such as vessels and bifurcations, in images. Other features such as DoP (“differences of paraboloids”),²⁰ SIFT (“scale-invariant feature transform”) or BRIEF (“binary robust independent elementary features”)²¹ could also be applied but are not considered in this evaluation. In the next step (*Step D*), a *local* frame-to-frame registration is performed along the determined track of the video-sequence. In a final step (*Step E*), a *global registration* process based on bundle adjustment corrects possible misalignments and provides a *loop-closing*.¹

Quality Criteria

As recently introduced in our preliminary work,⁹ an important quality criterion of a cystoscopic panorama image is its **completeness**, thus every region of the bladder that is observed with the cystoscope (0 degrees or 30 degrees, video cystoscope), should also be depicted in the corresponding panorama. Closely related to the completeness (no incomplete areas visible in the panorama) is the **extension**. In this paper, we use the **extension** as an approximate measure for the **completeness**. In order to evaluate those two criteria for the five phantoms, some geometrical assumptions were made. Since the bladder phantoms are mainly spherical objects, we defined an imaginary fixed point in the center of the observed hemisphere (termed the ‘south pole’) directly opposite to the insertion opening mimicking the urethra (termed ‘north pole’), see [Figure 3](#), left.

In a phantom that is assumed to be spherical, the **extension** can be assessed by the *degree of latitude* between the fixed point (being the ‘south pole’) and the maximum observable landmarks on the border of the panorama. It can be assumed, that with a rigid or flexible cystoscope, whose tip is located in the center of the sphere and moved using standard tilting, rotating, pushing and pulling maneuvers, the complete *distal hemisphere* is defined from the ‘south pole’ to the ‘equator’ at 90 degrees latitude, see [Figure 3](#), right. Hence, it is of special interest how far the panorama can be extended “*beyond the equator*”. Thus, for each panorama the **maximum extension** is approximated by the distance of a landmark furthest away (in degrees of latitude) from the ‘south pole’ ([Fig. 3](#) right, and [Table 1](#), center part). This angle limits the observed area. It is strongly dependent on the endoscope's viewing angle (0 or 30 degree) or bending possibilities (video-cscope), as well as the geometry, deformability and diameter of the entrance point (urethra) of the phantom.

The obtained panorama images are most often not exactly symmetrical ([Figs. 1](#) and [2](#)). This can be explained by a limiting angle depending on the **longitude** of the phantom. If this variation in symmetry is large, it might be an indicator that the stitching process will not work equally well for all areas within the phantom, especially if the panorama is extended beyond the equator.

To assess the *observed* area, it is also important to know the limits of the *observable* area: Due to the combination of (a) the geometry of the phantom (spherical or ellipsoid) and (b) the endoscope (0- or 30-degree view, video-cscope), some areas close to the urethra are generally unobservable. These positions can be determined by bending the endoscope to the outermost possible position or compressing the phantom's wall from the outside or by the partial inversion of the video-cscope. This is the optimal value that can be reached for any panorama. For a perfect

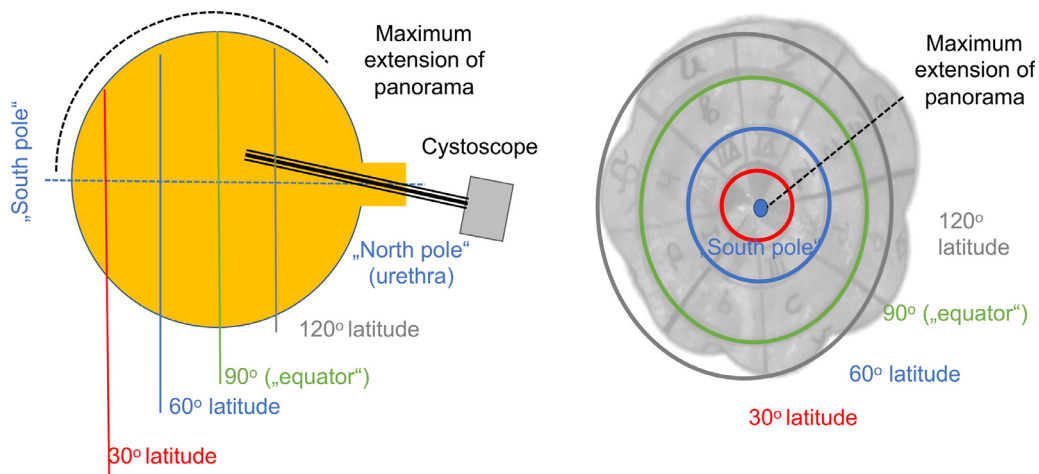


Figure 3. Left Side: Lateral sketch of a spherical phantom with denoted fixed points ('south pole') and urethra ('north pole') and degrees of latitude. The dotted line refers to a possible maximum extension of the generated panorama. Right side: Related virtual 2D panorama of a spherical phantom, with "south pole" and degrees of latitude marked. The dotted line refers to the maximum extension of the generated panorama, Figure from.⁹

panorama, the limits of the observed and the potentially observable area should fit for all longitudes.

One further important criterion for the evaluation of panoramic images is the **quality of the stitching process** itself. If the algorithm fails to extract a sufficient number of unique features, single tiles might be placed at the wrong position or are sheared or stretched in a wrong manner. While extreme shearing and the algorithm's affected tiles can be detected, misplaced frames are hard to detect automatically without a ground truth. Therefore, we inspected the resulting panorama images manually for stitching errors.

RESULTS

In our experiments, we were able to obtain panoramic images for all five phantoms with a 0-degree as well as with a 30-degree cystoscope. Furthermore, panoramic images for phantoms A, C and E were computed, using a flexible videoscope. Representative panorama images are depicted in Figure 2, second row (0-degree), third row (30-degree) and bottom row (videoscope). The cystoscope tip was moved from the center of the hemisphere ("south pole") to the border towards and beyond the "equator" (see Fig. 3) and backwards again. This motion was repeated with an angular shift resulting in star-shaped tracks and panoramas. The system tries to arrange the tiles in a way that optimizes the match between the single tiles, without distorting the original input patches more than necessary. This can cause slightly different projections and "equator" lines, depending on the phantom's geometry and the actual angle of the endoscope. The stitching algorithm was applied in an identical manner for all tests, except for the parameters regarding the diameter of the region of interest. We adapted this parameter to the different cystoscopic optical projections onto the camera. The used set of parameters has been previously shown to work well with the texture of real human bladders.² Due to the smaller image sensor with a VGA resolution at the tip of the flexible cystoscope, the image quality was not sufficient enough to provide adequate features needed for the panoramic stitching for phantoms B and D.

Approximating the maximum observation angles for phantom B was only possible with low precision, since the ringing

texture of the printed material and the additional applied vascularization landmarks of the 3D-printed phantom were not clearly visible. A similar problem exists for phantom E, where no latitude landmarks were visible inside. Thus, we used pairs of small, ball-shaped magnets (2 mm diameter) placed in- and outside of the phantom, in order to approximate the latitude with respect to the assumed 'south pole'. Phantom A incorporates only one vascularized hemisphere; hence latitude pen-markers were added on the proximal hemisphere. Table 1 (center) provides the *maximum observed degree of latitude* between the central landmark 'south pole' and the landmarks depicted in the periphery of the panorama (borders of the panorama). Table 1 (bottom) shows the number of *visible stitching errors* in relation to the *total number of frames* in the panorama image. Compared to our previous experiments⁹ with rigid cystoscopes and based on the improved algorithm, briefly described in Section "Panoramic Image Processing", the maximum observed angles for all phantoms could be enlarged, while the observable stitching errors could be reduced.

DISCUSSION

For four of the evaluated phantoms (A, C, D, E), we achieved very satisfying results. The computed panoramas depict wide areas of the phantom's observable inner surface. As can be seen in Figure 2 (second and third rows) where the 'equator' separates the distal and proximal hemispheres, all panoramas fully depict the distal hemisphere, using all three cystoscopes.

Unsurprisingly, the captured panorama images cover a larger part of the surface using the flexible videoscope than with the 30-degree side-view and the 0-degree frontal-view lens. The hand-drawn vascular texture in phantom A (acrylic glass) and phantom C provide a sufficient number of features for the stitching process, as well as the ruffle structures of phantoms D and E. For the cast-based silicon phantoms C and D (from Tübingen), the obtained angles in the panorama are close to the observable

maximum and are beyond the “equator”. *Phantom A* is a special case, since only the distal hemisphere has originally been covered with vascular texture features. Nevertheless, stitching worked also outside the painted part. For the experiments with the flexible cystoscope, additional vascular patterns were added on the proximal hemisphere (Fig. 2, bottom row, left image). The rate of stitching errors is low for all phantoms. Specifically, *phantom E* provides textures that mimic the inside of a bladder in a realistic manner. Despite that, fine grained textures and vessels are not present. Thus, it became necessary to use a larger distance between the endoscope tip and the phantom wall and a slightly altered path to register some regions with low feature density. *Phantom E* is flexible, and other than *phantom C* and *D*, its shape changes from elliptical to spherical through its own weight when filled with water as immersion fluid. This behavior closely resembles that of a real bladder during endoscopy.

Phantoms C, D and E are the ones allowing a water-filling during the examination. This causes small air bubbles on the inner surface of the phantoms. These were quite stable regarding their position and served as additional feature points for the stitching process. This partially reduced the problems with the missing vessel structure in these phantoms, which were sparser compared to *Phantom A* or real tissue but is not a realistic approach.

As can be seen in Table 1 (bottom part), in general, the rate of visible stitching errors is in most cases slightly higher for the 30° endoscope than with the other endoscopes. A closer look at the single tiles recorded by the device shows that the sharpness for these tiles is lower and there is more noise. Thus, the higher error rate here might be caused by the reduced recording quality. Summing up, the quality and extension of the resulting panoramas depend the following parameters: (a) the shape, color and texture, and deformability of the phantom bladder describing the “scene”, (b) the sensor characteristics (color, amount and size of the camera pixels) as well as the color temperature of the light source (LED, or xenon) which relate to the as incoming information, and (c) the movement of the cystoscope tip with respect to the bladder wall, which depends both on the stiffness and deformability of the phantom, as well as the experience of the user. Thus, there will never be exact same panoramas of the same scene.

CONCLUSION

We compared five bladder phantoms made of different materials, with different stiffness and various types of visible texture features or vascularization with respect to the hypothesis, whether their surface structure, stiffness, water-filling and geometry are suitable for the generation of panorama images. We obtained panoramic images for all five phantoms with the rigid cystoscopes (0° and 30° angle) and for phantoms A, C, and E using the video-scope. The ringing structure typical for 3D prints (phantom B) does not provide sufficient texture to support the stitching process, and furthermore, the reflective surfaces

as in the 3D-printed phantoms *D* and *E* may cause problems. Engraved and painted patterns (phantoms A, C and D) on the surface work equally well. The three deformable phantoms (C, D and E) yield larger panoramas than the static phantoms (A and B) as they allow the option to artificially extend the viewing options. As the image sensor at the distal end of the flexible videoscope integrates a much smaller number of pixels than the proximal cameras used with rigid endoscopes, the related image quality was not sufficient enough to provide adequate features needed for the panoramic stitching for phantoms B and D.

As expected, the flexible cystoscope provided panoramas with larger extensions with up to ~330°, than the rigid side- and frontal-view 30° and 0°- endoscopes yielding a maximum visible range of up to ~300° and ~270°, respectively.

Also, as the internal model of the stitching process assumes as spherical object which is projected on a plane (Fig. 1), all image regions “beyond the equator” become heavily deformed and distorted, meaning that even if regions near the urethra (north pole) can be captured by the cystoscope, the stitching and projection process becomes challenging.

A still open challenge is the design and construction of an optimal new phantom that includes the anatomical geometry of an empty bladder (as with phantoms B and E), allows water filling to resemble the procedure of a standard cystoscopy (as with phantoms C, D and E), a deformable geometry from elliptical to spherical (as with phantom E) and a suitable real-type vascular texture in the inside (as in phantom A and in real data as depicted in Fig. 1).

ACKNOWLEDGMENT

This work has partially been supported by the German Ministry for Research and Education (BMBF) under the contract 03ZZ0444E (subproject “Interactive visualization of 2D/3D panorama endoscopy data of the bladder”) within the Project “3D-Sensation – Uro-MDD”.

References

1. Bergen T. *Real-Time Endoscopic Image Stitching for Cystoscopy*. Univ. Koblenz; 2017. PhD Thesis.
2. Kriegmair M, Bergen T, Ritter M, et al. Digital mapping of the urinary bladder: potential for standardized cystoscopy reports. *Urology*. 2017. pii:S0090-4295(17) 30151-6.
3. Wittenberg T, Brischwein M, Nowack S, Chen G, Bergen T. Panorama-Bildgebung der Blase: Vom Phantom zu Präklinischen Experimenten. *Endoskopie Heute*. 2014;27:146–150.
4. Kuronen-Stewart C, Ahmed K, Aydin A, et al. Holmium laser enucleation of the prostate: simulation-based training curriculum and validation. *Urology*. 2015;86:639–646. <https://doi.org/10.1016/j.urology.2015.06.008>. Epub 2015 Jun 27.
5. Available at: <https://www.somso.de/en/anatomie/medizinischephantome/urology-catheterisation/ts-64/>.
6. Michel M, Knoll T, Köhrmann K, Alken P. The URO Mentor: development and evaluation of a new computer-based interactive training system for virtual life-like simulation of diagnostic and therapeutic endourological procedures. *BJU Int*. 2002;89:174–177. <https://doi.org/10.1046/j.1464-4096.2001.01644.x>.
7. Shah M, Aydin A, Moran A, Khan MS, Dasgupta P, Ahmed K. The role of cognitive training in endourology: a randomized controlled

- trial. *Actas Urológicas Españolas (English Edition)*. 2018;42:163–169. ISSN 2173-5786.
8. Hamacher A, Whangbo TK, Kim SJ, Chung KJ. Virtual reality and simulation for progressive treatments in urology. *Int Neurourol J*. 2018;22:151–160. <https://doi.org/10.5213/inj.1836210.105>.
 9. Hackner R, Grund KE, Franz D, Müller PF, Lemke N, Wittenberg T. Evaluation of different bladder phantoms for panoramic cystoscopy. In: Burgert O, Hirt B, eds. *Proc's 18th Annual Meeting Deutsche Gesellschaft für Computer- und Roboterassistierte Chirurgie (CURAC 2019)*. 2019:247–252.. Available at: https://www.curac.org/images/advportfoliopro/images/CURAC2019/Tagungsband_Im-pressum_Curac.pdf.
 10. Péntek Q, Hein S, Miernik A, Reiterer A. Image-based 3D surface approximation of the bladder using structure-from-motion for enhanced cystoscopy based on phantom data. *Biomed Eng*. 2018;63:461–466.
 11. Lurie KL, Smith GT, Khan SA, Liao JC, Ellerbee JC. Three-dimensional, distensible bladder phantom for optical coherence tomography and white light cystoscopy. *J Biomed Opt*. 2014;19: 036009.. Available at: <https://www.ncbi.nlm.nih.gov/pmc/articles/PMC3951584/pdf/JBO-019-036009.pdf>.
 12. Pfeifle M, Born S, Fischer J, et al. VolV - Eine OpenSource-Plattform für die Medizinische Visualisierung. In: *Proc's 6th Annual Conf. German Society for Computer- and Robot-assisted Surgery (CURAC)*. 2007:193–196.
 13. Li D, Suarez-Ibarrola R, Choi E, et al. Soft phantom for the training of renal calculi diagnostics and lithotripsy. In: *Proc's 41st Annual Int. Conf. IEEE Engineering in Medicine and Biology Society (EMBC)*. 2019:3716–3719.
 14. Adams F, Qiu T, Mark A, et al. Soft 3D-printed phantom of the human kidney with collecting system. *Ann Biomed Eng*. 2017;45:963–972. <https://doi.org/10.1007/s10439-016-1757-5>.
 15. Hackner R, Hann A, Meining A, Raithel M, Wittenberg T. Panoramic endoscopy of the stomach: first results from phantom and patient data. In: Neumuth T, Melzer A, eds. *Proc's 17th Annual Conf. German Society for Computer- and Robot-assisted Surgery (CURAC)*. 2018:247–252. Available at: <https://www.curac.org/images/advportfoliopro/images/CURAC2018/CURAC%202018%20Tagungsband.pdf>.
 16. Bergen T, Hastreiter P, Xu T, et al. Real-time panorama imaging of sphenoid sinuses from monocular endoscopic views: an update based on clinical experiments. In: Feussner H, ed. *Proc's 13th Annual Conf. German Society for Computer- and Robot-assisted Surgery (CURAC)*. 2014:32–35.
 17. Schuster M, Bergen T, Reiter M, Münzenmayer C, Friedl S, Wittenberg T. Laryngoscopic image stitching for view enhancement and documentation - first experiences. *Biomed Eng Biomed Tech*. 2012;57 (S1):704–707.. Available at: <http://citeseerx.ist.psu.edu/viewdoc/summary?doi=10.1.1.652.5139>.
 18. Bergen T, Wittenberg T, Münzenmayer C. Shading correction for endoscopic images using principle color components. *Int J Comput Assist Radiol Surg*. 2016;11:397–405. <https://doi.org/10.1007/s11548-015-1273-3>.
 19. Bay H, Ess A, Tuytelaars T, van Gool. SURF: speeded up robust features. *Comput Vis Image Underst*. 2008;110:346–359.
 20. Bergler M, Weiherer M, Bergen T, et al. Stitching pathological tissue using DOP feature tracking. In: Maier A, Deserno T, Handels H, Maier-Hein K, Palm C, Tolxdorff T, eds. *Bildverarbeitung für die Medizin 2018*. 2018:322–327.. Available at: https://link.springer.com/chapter/10.1007/978-3-662-56537-7_84.
 21. Nowack S, Wittenberg T, Paulus D, Bergen T. Merkmalsverfolgung für die Panoramaendoskopie. In: *Proc's Bildverarbeitung für die Medizin 2013*. 2013:205–210.. Available at: https://link.springer.com/chapter/10.1007/978-3-642-36480-8_37.
 22. Choi E, Waldbillig F, Jeong M, et al. Soft Urinary Bladder Phantom for Endoscopic Training.. *Ann Biomed Eng*. 2021. <https://doi.org/10.1007/s10439-021-02793-0>.